YALE
PEABODY
MUSEUM

P.O. BOX 208118 | NEW HAVEN CT 06520-8118 USA | PEABODY.YALE. EDU

JOURNAL OF MARINE RESEARCH

The *Journal of Marine Research,* one of the oldest journals in American marine science, published important peer-reviewed original research on a broad array of topics in physical, biological, and chemical oceanography vital to the academic oceanographic community in the long and rich tradition of the Sears Foundation for Marine Research at Yale University.

An archive of all issues from 1937 to 2021 (Volume 1–79) are available through EliScholar, a digital platform for scholarly publishing provided by Yale University Library at https://elischolar.library.yale.edu/.

Requests for permission to clear rights for use of this content should be directed to the authors, their estates, or other representatives. The *Journal of Marine Research* has no contact information beyond the affiliations listed in the published articles. We ask that you provide attribution to the *Journal of Marine Research.*

Yale University provides access to these materials for educational and research purposes only. Copyright or other proprietary rights to content contained in this document may be held by individuals or entities other than, or in addition to, Yale University. You are solely responsible for determining the ownership of the copyright, and for obtaining permission for your intended use. Yale University makes no warranty that your distribution, reproduction, or other use of these materials will not infringe the rights of third parties.

On turbulence and normal modes in a basin

by J. H. LaCasce[1]

ABSTRACT

The problem of forced, geostrophic turbulence in a basin is revisited. The primary focus is the time dependent field, which is shown to be approximately isotropic (in contrast to the strongly zonally anisotropic fields seen in periodic domains). It is also approximately homogeneous, away from the boundaries. Phenomenological arguments suggest the isotropy occurs because the inverse cascade of energy is arrested by basin normal modes rather than by free Rossby waves. Peaks in the velocity spectra at modal frequencies are consistent with basin modes, as has been noted previously. We discuss which modes would be excited and whether dissipation or the mean flow would be expected to alter the modes and their frequencies.

A relatively novel feature is the use of Eulerian velocity statistics to quantify the wave and turbulence characteristics. These measures are more suitable to this environment than measures like wavenumber spectra, given the inhomogeneities associated with the boundaries.

With regards to the mean, we observe a linear $\langle q \rangle - \langle \psi \rangle$ relation in the region of the mean gyres (at the northern and southern boundaries), consistent with previous theories. This is of interest because our numerical advection scheme has implicit rather than explicit small scale dissipation, and requires no boundary conditions on the vorticity. The gyre structure is however somewhat different than in an (inviscid) Fofonoff-type solution, suggesting dissipation cannot be neglected.

1. Introduction

Random forcing at small scales can drive a large-scale response in nondivergent, two-dimensional flows (Onsager, 1949; Fjørtoft, 1953; Batchelor, 1953; Kraichnan, 1967). This "inverse cascade" of energy owes its existence to the joint conservation of energy and enstrophy in the absence of dissipation. It is significantly affected by the β-effect, slowing greatly or "arresting" at a scale at which Rossby waves are dynamically competitive with advective processes (Rhines, 1975; Holloway and Hendershott, 1977). Reviews of these processes and related topics can be found in Kraichnan and Montgomery (1980), Rhines (1979) and Holloway (1986).

Commonly observed in arrested 2-D β-turbulence are zonally anisotropic structures or "jets" (Rhines, 1994). These are long-lived features which can span the domain and have a meridional scale that varies with β. They occur because the arrest to Rossby waves is

1. Woods Hole Oceanographic Institution, M.S. 29, Woods Hole, Massachusetts, 02543, U.S.A. *email: jlacasce@whoi.edu*

inherently anisotropic; this is clearly illustrated in a phenomenological argument due to Vallis and Maltrud (1993), as follows.

The vorticity of a barotropic fluid on the β-plane evolves according to:

$$\frac{\partial}{\partial t} \nabla^2 \psi + \mathbf{u} \cdot \nabla(\nabla^2 \psi) + \beta \frac{\partial}{\partial x} \psi = \mathcal{F} - \mathcal{D} \tag{1}$$

where ψ is the velocity streamfunction ($\mathbf{u} = \hat{k} \times \nabla \psi$) and $\mathcal{F}$ and $\mathcal{D}$ the forcing and dissipation. Solutions to (1) without forcing, dissipation or nonlinearity can be expressed as a superposition of Rossby waves with dispersion relation:

$$\omega = -\frac{\beta k}{k^2 + l^2} \equiv -\frac{\beta k}{\kappa^2}, \tag{2}$$

where k, l and κ are the zonal, meridional and total wavenumbers, respectively.

With forcing and nonlinearity, it is possible to achieve a statistical steady state in which energy injected at small scales cascades to larger scales and is dissipated. Rossby waves hinder this process by slowing the cascade; then energy accumulates at the "Rhines scale" where the time scale of the turbulence and the waves are comparable. In the energy inertial range, assuming a constant rate of energy transfer, ϵ, the turbulence time scale is proportional to $\epsilon^{-1/2} \kappa^{-2/3}$; equating this and the wave period yields an estimate for the arrest wavenumber:

$$\kappa_\beta = C\left(\frac{\beta^3}{\epsilon}\right)^{1/5} \cos^{3/5}(\theta), \tag{3}$$

where θ is the angle between the wave vector and the k-axis and C is an order unity constant.[2]

Relation (3) defines a transition curve which effectively separates "turbulent" and "wave-like" wavenumbers. It is anisotropic because $\kappa_\beta = C(\beta^3/\epsilon)^{1/5}$ if $\theta = 0$, but $\kappa_\beta = 0$ if $\theta = \pi/2$. The latter corresponds to $k = 0$, i.e. zonally invariant modes. In physical terms, Rossby waves are unable to prevent a cascade to the $k = 0$ modes because waves with $k = 0$ have zero frequency.

The occurrence of zonal jets in turbulence simulations has been well documented, in doubly periodic domains (e.g. Rhines, 1979; Panetta, 1993), in re-entrant channels (McWilliams *et al.,* 1978; Treguier and McWilliams, 1990) and on the sphere (Williams, 1978; Cho and Polvani, 1996; Nozawa and Yoden, 1997; Huang and Robinson, 1998). Jets in other words have been found in any domain which is zonally re-entrant. They have been invoked to explain similar structures in the Jovian atmosphere, in the earth's atmosphere and in the ocean.

Most ocean basins of course are not zonally reentrant, and meridional boundaries are

---

2. An alternate expression, like that of Rhines (1975), is obtained if one uses the rms velocity to estimate the turbulence time scale; then $\kappa_\beta \propto (\beta/U)^{1/2}$, i.e. the inverse inertial boundary layer width.

likely to affect jets in the least by preventing their reconnection. But boundaries can also hinder the energy cascade by breaking the conservation of enstrophy (Rhines, 1975). The equation for the domain-integrated enstrophy, obtained from (1) without forcing or dissipation, is:

$$\frac{1}{2}\frac{\partial}{\partial t}\int\int (\nabla^2\psi)^2 dxdy = \frac{\beta}{2}\left(\int_{west} v^2 dy - \int_{east} v^2 dy\right),\qquad(4)$$

where v is the meridional velocity (assuming the boundaries run north-south and there is no normal flow at the walls). Eq. (4) implies the western boundary is a source of enstrophy and the eastern boundary a sink, and it is the generation of small-scale structure in the west which could hinder a cascade to large scales.

Two dimensional turbulence in basins has been examined extensively, both without and with forcing. Veronis (1970) considered how time-dependent forcing altered the mean flows he obtained earlier in simulations with steady forcing (Veronis, 1966). Later, Bretherton and Haidvogel (1976) and Salmon *et al.* (1976) used the calculus of variations and statistical mechanics, respectively, to reach the same conclusion: that turbulence in a basin should drive a rectified flow like Fofonoff's (1954) free mode solution; the Fofonoff mode is a state of minimum enstrophy in the first case, and of maximum entropy in the second.[3] The rectified mean is characterized by an anticyclonic gyre at the northern boundary and a cyclonic gyre at the southern; i.e., like the gyres described by Veronis (1966). The relative strengths of the gyres can vary; in the symmetric case, the mean has zero integrated vorticity.

The rectified mean was examined subsequently by several authors (Griffa and Salmon, 1989; Griffa and Castellari, 1991; Cummins, 1992; Wang and Vallis, 1994; Dukowicz and Greatbatch, 1999; Greatbatch and Nadiga, 2000). In general, the resemblance to a Fofonoff mode varies, depending on the forcing and damping as well as on the boundary conditions. But it is a nearly ubiquitous feature in turbulent basins, with β.

Some of these authors also examined the time-dependent flow in the basin interior. This is the primary focus of the present work and we will consider several aspects. The first is the inverse cascade of energy; that such a cascade proceeds unambiguously with small-scale forcing (despite enstrophy production in the west) has been indicated previously (Griffa and Castellari, 1991; Seidov and Marushkevich, 1992), but further quantitative evidence will be presented here.

The second concerns isotropy in the interior. The evidence from previous works on this point is not conclusive. The instantaneous streamfunction fields of Griffa and Salmon (1989) appear nearly isotropic, but Seidov and Marushkevich (1992) display zonally anisotropic features. The laboratory experiments of Colin de Verdiere (1980) in a square basin yielded

---

3. That the two approaches produce the same result in the limit of infinite resolution, i.e. when the smallest resolved scale vanishes, was demonstrated by Carnevale and Fredericksen (1987).

approximately isotropic features, as did the numerical experiments of Spall (2000). In the least, there are several indications that the arrest in the basin may be different than in a zonally periodic domain.

Why might this be so? There is evidence that the cascade in a basin is halted not by free Rossby waves but by basin normal modes (Griffa and Castellari, 1991). If so, the arrest might be very different because basin modes have a different dispersion relation:

$$\omega_{nm} = \frac{\beta}{2\pi(n^2/L_x^2 + m^2/L_y^2)^{1/2}}, \tag{5}$$

where n and m are zonal and meridional (integral) wavenumbers. Unlike (2), (5) is *symmetric* in the wavenumbers, assuming $L_x \approx L_y$. Using (5) we obtain an estimate for the (quantized) arrest wavenumber:

$$\kappa_{nm} = C\beta^{3/5}\epsilon^{-1/5}, \tag{6}$$

where $\kappa_{nm} \equiv 2\pi(n^2/L_x^2 + m^2/L_y^2)^{1/2}$. Unlike (3), relation (6) is isotropic. If basin modes are important, the basin arrest might also be isotropic.

Hereafter we examine these issues via forced numerical simulations in a square basin; results from a periodic model will be used for comparison. A point which distinguishes this study from similar 2-D turbulence studies is the means of measurement: rather than using wavenumber spectra (as is common with periodic fields, but problematic with inhomogeneities), we will use Eulerian velocity statistics. These are well suited for this environment (and could conceivably be used with oceanographic data).

2. Models

The numerical model solves Eq. (1). The code uses finite differences to calculate spatial derivatives and sine transforms to invert the Poisson equation relating the vorticity, $\nabla^2\psi$, and the streamfunction. Time stepping is third-order Adams-Bashforth. The forcing was a white-in-time stochastic function applied over a specified range of wavenumbers (a random field was generated in wavenumber space and converted to real space via the inverse sine transform).

The forcing was applied at large wavenumbers, from $\kappa = 30$ to 35, so that the inverse cascade span a range of scales. Zonal and meridional wavenumbers were excited equally (the forcing was isotropic). Dissipation was by a linear drag, to simulate a bottom Ekman layer, and the basin was taken to be square. The rigid lid approximation implies that $\psi = const.$ on the boundaries, and this constant can be taken to be zero without loss of generality.

A somewhat unusual feature is the model's advection scheme. This is a 2-D version of the QUICK scheme of Leonard (1979), a third-order, upwind scheme. Because it upwinds, it is more stable to small-scale oscillations than center-difference schemes, and because it is third-order, it is more accurate than second order schemes. However, it does have an

associated diffusion which acts at small scales (e.g. Ferziger and Peric, 1999). This diffusion is implicit and fourth-order, equivalent to biharmonic diffusion.

An important advantage of this implicit diffusion, compared with explicitly imposed dissipation, is that *no additional boundary conditions need be specified* (e.g. Becker and Salmon, 1997). In addition, the effective viscosity is proportional to the local velocity which means that the dissipation at the boundaries is *along* rather than perpendicular to the boundary. These aspects will turn out to be important with regards to the mean flow. There are of course other finite difference advection schemes available (e.g. Lele, 1992; Shchepetkin and McWilliams, 1998), some with higher order accuracy than the QUICK scheme. The present results were in any case checked at low and higher resolution and those phenomena discussed hereafter are robust.

The spectral model, used for comparisons, was written by G. Flierl. It also solves Eq. (1) with periodic boundary conditions in x and y. Advection follows Patterson and Orszag (1971), but without dealiassing; the latter produced nearly negligible changes in the results but required significantly longer computations. This model also employs third-order AB time stepping.

For the basin experiments, we used 512^2 grid points. Experiments with coarser resolution (256^2 grid points) were made to define parameter ranges. With the periodic model we used 256^2 Fourier modes (and thus 256^2 grid points). Spectral models are more accurate for spatial differencing than finite element models, and comparing the 256^2 mode periodic experiments with the 512^2 grid basin runs appeared to be reasonable.

Both model domains had a dimensionless width of π (so distances are directly comparable between the two). The β and dissipation parameters given hereafter are scaled appropriately, assuming velocities are order one. For reference, a value of $\beta = 100$ yields an inertial boundary layer width, δ_I, which is about one tenth the basin width, and a Stommel boundary layer width, δ_S, comparable to the grid spacing; δ_S is thus two orders of magnitude smaller than δ_I. With regards to dimensional values, the basin has a width of $1000L \approx 3000$ km if $\beta = 100$ and $U \approx 20$ cm/sec.

3. Mean flow

The model was run to a statistical steady state and then onwards for roughly a hundred eddy turnover times. As in the aforementioned studies, mean flows develop. There are several points here which are worth discussing before proceeding to the time dependent fields.

Representative examples of the mean streamfunction and relative vorticity are shown in the upper panels of Figure 1. As expected, the mean has a dual gyre structure, anticyclonic at the northern boundary and cyclonic at the southern. The gyres are nearly zonally symmetric and of a meridional extent comparable to the inertial boundary layer width. The gyre vorticity associated is strongly boundary-trapped, negative in the north and positive in the south.

Statistical mechanics predicts a linear relation between the mean potential vorticity and
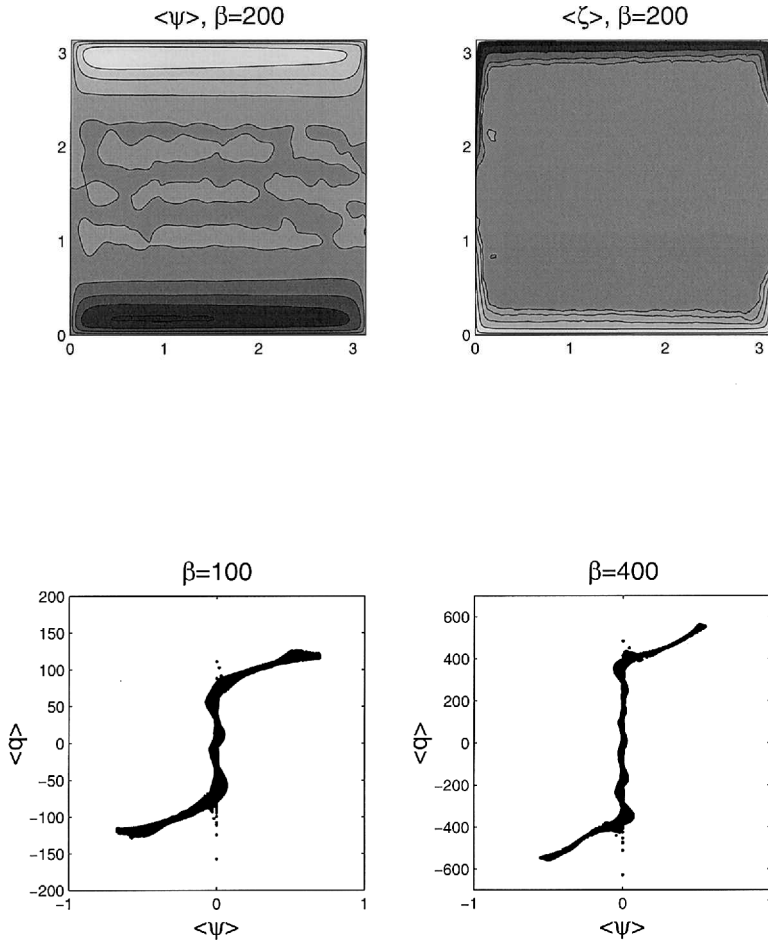
Figure 1. The mean fields. The mean streamfunction and relative vorticity for the β = 200 experiment are in the upper panels. The contour values are [−.6 −.4 . . . .4 .6] for the streamfunction and ±[150 100 50 10]. The $q − \psi$ scatter plots for the means from experiments with β = 100 and 400 are shown in the lower panels.

the mean streamfunction (Salmon *et al.,* 1976); the slope moreover should be positive (in which case the mean is also nonlinearly stable; Carnevale and Fredericksen, 1987). Scatter plots of $\langle q \rangle − \langle \psi \rangle$ are shown in the lower panels and in the gyre regions, there is a nearly linear dependence between $\langle q \rangle$ and $\langle \psi \rangle$, with a positive slope; outside the gyres, the streamfunction is essentially zero.

First, we note that the linear $\langle q \rangle − \langle \psi \rangle$ relation obtains with our advection scheme. Previous works (Cummins, 1992; Wang and Vallis, 1994; Dukowicz and Greatbatch, 1999) suggest the $\langle q \rangle − \langle \psi \rangle$ relation depends on the boundary conditions. With no slip or free slip boundary conditions, the linear relation does not obtain; the gyres rather have
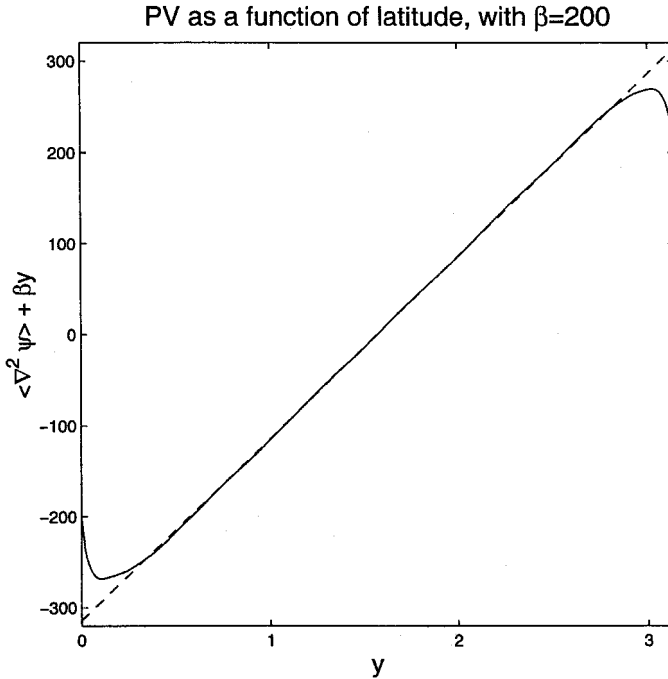
Figure 2. The mean potential vorticity as a function of latitude for $\beta = 200$ at the basin midline. Note the lack of plateaus, as would be expected if the gyres were homogenized. The profiles at other values of x are nearly identical (except in the western boundary layer).

homogenized PV; only with "super-slip" boundary conditions (in which the gradient of the vorticity vanishes at the boundary rather than the vorticity, Marshall, 1984) is the linear relation recovered. In all the cited works, the small-scale dissipation was explicit, either Laplacian or biharmonic diffusion.

Our small-scale dissipation in contrast is implicit, with no boundary conditions on the vorticity imposed. Perhaps more importantly though, the viscosity acts parallel to the local velocity (Sec. 2). As such, numerical diffusion across the mean contours should be greatly reduced, provided the mean accounts for a substantial fraction of the instantaneous velocity. We find no evidence of homogenization. Shown in Figure 2 is a slice in y of the PV from the run with $\beta = 200$; no plateau is seen. The linear $\langle q \rangle - \langle \psi \rangle$ relation holds in the gyres.

This result suggests that the previously documented homogenization might be related to explicit small-scale dissipation. Diffusion across mean contours is the means by which PV is homogenized (Rhines and Young, 1982), and it is plausible that small-scale diffusion could accomplish this, given the steep mean vorticity gradients (Fig. 1). Consistent with this notion, Wang and Vallis (1994) found increased homogenization with decreasing Reynold's number. Perhaps also consistent is that Griffa and Salmon (1989), who used the

"anticipated vorticity method" (Sadourny and Basdevant, 1985) to dissipate small-scale variance, did *not* observe homogenization.

But the situation may indeed be more complicated. Greatbatch and Nadiga (2000) used Laplacian diffusion of vorticity in their experiments but found it was insignificant to the vorticity balance integrated over a region bounded by a mean streamline; rather, the forcing was balanced by the Reynolds flux of vorticity, which evidently acted like down gradient diffusion. The authors used steady forcing (in contrast to the present stochastic forcing with zero mean curl). But Griffa and Salmon also used steady forcing and found $\langle q \rangle - \langle \psi \rangle$ relations like those in Figure 1. Clearly further work is required, but explicit dissipation could be behind the documented homogenization, at least in part.

The second point concerns how the gyres compare to a Fofonoff-type solution. The gyres are *localized* in that they do not extend to the domain equator (see also Griffa and Castellari, 1991; Cummins, 1992 and Wang and Vallis, 1994), but a solution with similar structure can be constructed. Consider the northern boundary. Given the small variations in x, particularly at the domain center, the linear $\langle q \rangle - \langle \psi \rangle$ relation reduces approximately to an ODE:

$$\psi_{yy} + \beta y \cong A^2 \psi + \beta y_0, \tag{7}$$

where A^2 is the slope of the $\langle q \rangle - \langle \psi \rangle$ relation and y_0 is a reference latitude. We will impose $\psi = 0$ at the northern wall, $y = y_N$, and at the southern extent of the gyre, $y = y_S$. If the reference latitude is taken to be the southern edge of the gyre, the relative vorticity vanishes there. Then the solution is:

$$\psi = -\frac{\beta \Delta y \, \sinh\left(A(y - y_S)\right)}{A^2 \, \sinh\left(A\Delta y\right)} + \frac{\beta}{A^2}(y - y_S), \tag{8}$$

where $\Delta y \equiv y_N - y_S$ is the meridional extent of the gyre and y_N is the latitude of the northern wall. The solution's relative vorticity is negative at y_N, and if one matches its value to that observed in the numerical experiment, say r_N, one obtains the gyre width:

$$\Delta y = \frac{|r_N|}{\beta}. \tag{9}$$

(Scaling this relation, with $r_n \propto U/\Delta y$, shows $\Delta y \propto (U/\beta)^{1/2}$, the inertial boundary layer width.) From the experiment with $\beta = 200$ we have $r_N \approx -130$, which yields a gyre width $\Delta y \approx 0.65$, a reasonable estimate (Fig. 1).

However, the predicted and observed mean zonal velocities are intriguingly different. Examples of the zonal velocity from the Fofonoff solution (8), evaluated using parameters A and r_N from the simulations, are plotted against latitude in Figure 3. The velocity is eastward at the boundary but asymptotes to a constant westward value near the southern part of the gyre. The velocity is discontinuous here, dropping abruptly to zero to the south (the discontinuity is unavoidable with the present solution).

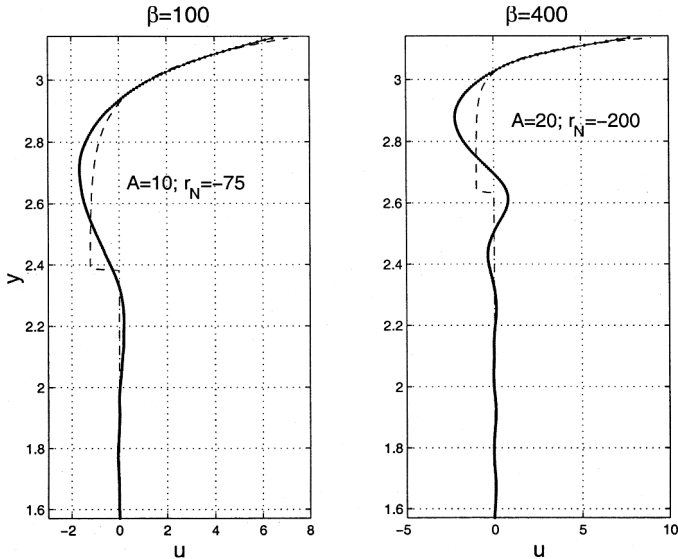The computed means (the dotted lines in the figure) are likewise eastward at the

Figure 3. The mean velocities from the basin midpoint to the northern wall along the basin midline, for two values of β. The observed velocity (solid) and that predicted from a local Fofonoff solution (dashed) are shown. The meridional velocity is not different from zero in either case.

boundary, but the westward flow is more jet-like. With larger values of β (e.g. the right panel) one even finds flow reversals, that is, additional eastward and westward jets. The velocity decays smoothly to zero in the south, yielding no discontinuity.

Because the oscillatory decay is absent in the inviscid solution, it is probably related to the linear drag. To demonstrate that conclusively however would require solving the nonlinear steady problem with dissipation, for instance using Newton's method (e.g. Cessi *et al.,* 1987); this is beyond the present scope.

How does the gyre localization fit in with statistical mechanics? The latter predicts a Boltzmann-like probability distribution under the assumption of ergodicity in phase space; the $\langle q \rangle - \langle \psi \rangle$ relation follows (Salmon *et al.,* 1976). We know however that β can prevent ergodicity, by inhibiting the meridional excursion of fluid parcels (Shepherd, 1987). With increasing β, ergodicity evidently only holds near the boundaries, where the accumulated vorticity is great enough to overwhelm the β-effect.

In any event, the present means are largely in accord with those found previously, so we will move on to the time-dependent fields. But we will return to the mean later, to see how it affects the basin modes.

4. Cascades

Several features of the time-dependent field can be seen clearly in snapshots of the streamfunction; examples for two values of β are shown in Figure 4. In both cases, we see
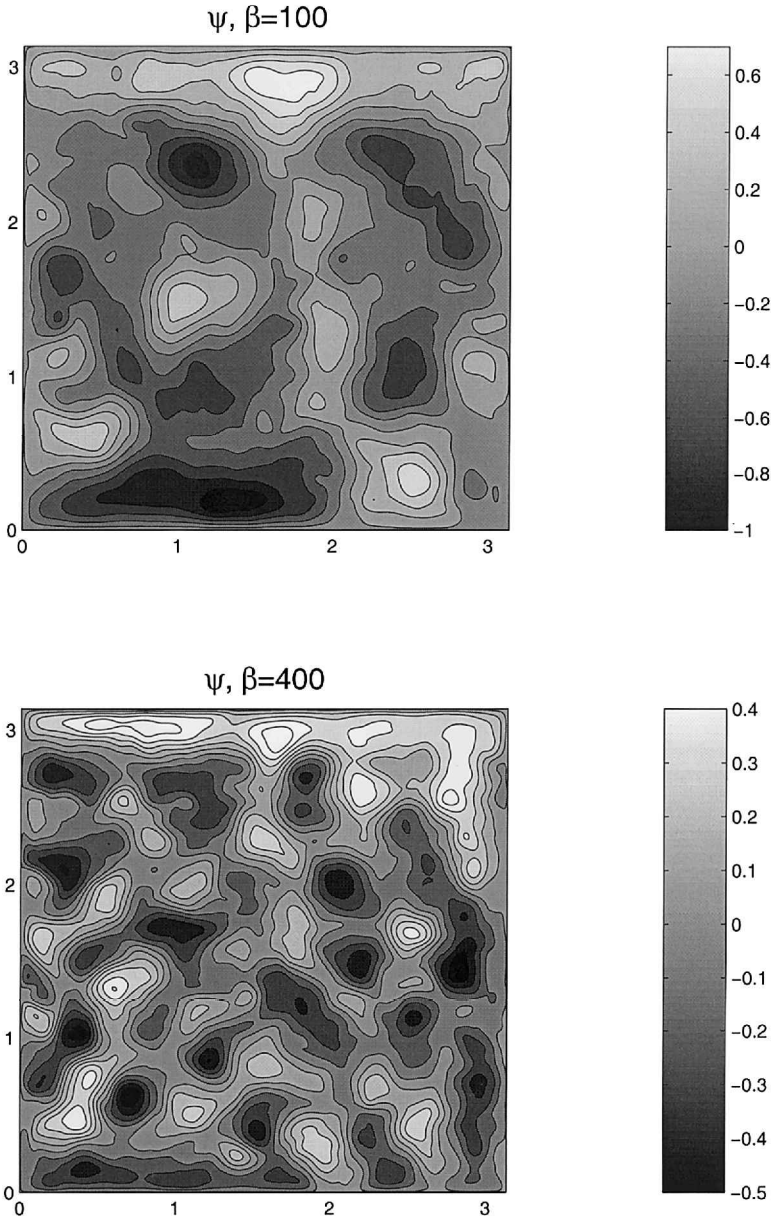
ψ, β=100

ψ, β=400

Figure 4. Snapshots of the streamfunctions from experiments with $\beta = 100$ and 400. The contour ranges are indicated.

the mean gyres discussed above, as well as eddies. The means and eddies are comparably strong, and the eddies are as large as the gyres are wide.

The eddies moreover are larger than the forcing scales, the largest of which is $\pi/30 \approx$

0.1; this is consistent with an inverse cascade. The eddies with $\beta = 100$ are larger than those with $\beta = 400$, consistent with an arrest due to β. That the eddies are as big as the gyres are wide means the eddies scale with the inertial boundary layer width, and therefore with the arrest scale (Sec. 1). Lastly, the eddies are largely isotropic in the interior; no jets are observed there.

The corresponding vorticity fields (not shown) exhibit more small-scale structure, as is usual. Besides the negative and positive vorticity at the northern and southern walls, there is also a western boundary region, with a width comparable to the northern and southern boundary layers. There one finds vortices of both signs.

So the instantaneous fields are consistent with an inverse cascade and with β limiting that cascade. But how do we quantify these observations? The most common approach is with wavenumber spectra but such a measure, which involves spatial averages, is problematic due to the inhomogeneities associated with the western, northern and southern boundaries.

Consider for example the time averaged, two-dimensional wavenumber spectrum of the enstrophy from a run with $\beta = 100$ (Fig. 5). The spectrum represents the mean square amplitudes from the 2-D sine transform of the relative vorticity. It exhibits several peaks with a zonal wavenumber of 1, from which we would infer a strongly zonally anisotropic field.

However, these peaks merely reflect the pools of vorticity at the northern and southern boundaries; indeed, the mean vorticity has practically the same spectrum. This is why the peaks have only even values of n_y, since those modes are asymmetric about the basin equator. Little can be learned about the basin interior from this spectrum.

The instantaneous fields however suggest the interior is approximately homogeneous, so we might proceed instead by calculating statistics there. Hereafter, various turbulence characteristics will be obtained solely from velocity records from the interior.

Velocities were saved at a number of grid points, mostly along the zonal and meridional center lines although other locations were also sampled. The temporal sampling rate was chosen in order to resolve in detail the dominant frequencies (Sec. 6).

We begin with the energy and enstrophy cascades, and velocity structure functions. The latter are moments of velocity differences between separated points and are familiar in 3-D turbulence studies (e.g. Batchelor, 1953; Frisch, 1995). Structure functions have been used to study the 3-D energy inertial range in the atmospheric boundary layer (Van Atta and Chen, 1970) and in the marine boundary layer (Van Atta and Park, 1980). They have also been examined in the context of 2-D cascades in the upper troposphere/lower stratosphere (Lindborg, 1999). Structure functions offer several advantages over wavenumber spectra, for instance by obviating the need to break the data into bins and remove individual mean velocities. And the connection between flow statistics and separation distance is more direct than with wavenumber spectra.

The variation of the *n*-order structure function with separation for 2-D turbulence can be deduced by dimensional analysis, although an exact relation can be derived for the third
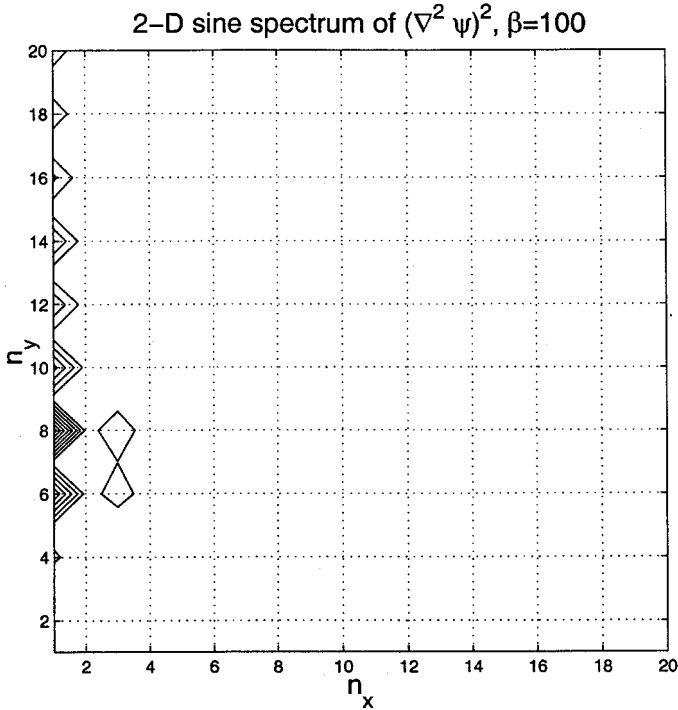
Figure 5. The squared amplitudes of the Fourier sine transform elements for the vorticity for the experiment with $\beta = 100$. The amplitudes have been normalized by the total enstrophy and thus the contours have dimensionless values (and so are not shown). Note the apparent zonal anisotropy, and that the peaks occur at even values of n_y.

order function (Lindborg, 1999).[4] Consider the second order functions first. Assuming a constant rate of energy transfer, ϵ, across the inertial range, dimensional arguments yield:

$$\langle(\delta v)^2\rangle = \langle(v(\mathbf{x} + \zeta) - v(\mathbf{x}))^2\rangle = C_{2\epsilon}\epsilon^{2/3}\zeta^{2/3}, \tag{10}$$

where $C_{2\epsilon}$ is a constant and ζ the separation between observations. Relation (10) applies to both longitudinal and transverse velocity differences (i.e. parallel and perpendicular to the line connecting the observers), albeit with different C_2. Relation (10) can be shown to be consistent with a $k^{-5/3}$ wavenumber spectrum.

In the enstrophy inertial range, we have:

$$\langle(\delta v)^2\rangle = C_{2\eta}\eta^{1/3}\zeta^2, \tag{11}$$

where η is the enstrophy dissipation rate and $C_{2\eta}$ another constant.[5] Relation (11) corresponds to a k^{-3} energy wavenumber spectrum.

---

4. The corresponding result in 3-D turbulence is Kolmogorov's (1941) well-known "4/5 Law."
5. A logarithmic correction has been suggested by Lindborg (1999).
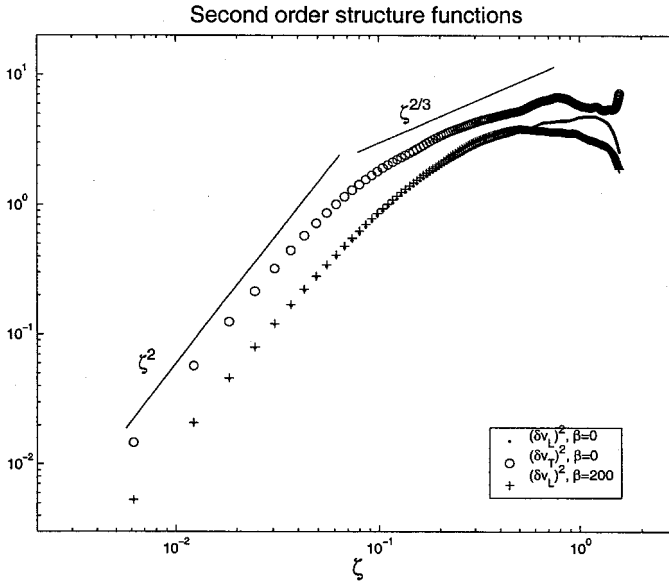
Second order structure functions

Figure 6. The second-order longitudinal and transverse structure functions from a run with $\beta = 0$; also shown is the longitudinal function from a run with $\beta = 200$. The curves were obtained by averaging the corresponding curves in the zonal and meridional directions relative to the basin center. The power laws indicate dependences expected in enstrophy and energy inertial ranges.

Second-order structure functions at the basin center are shown in Figure 6 for runs with $\beta = 0$ and $\beta = 200$. The curves were obtained by averaging from the zonal and meridional grid lines the corresponding curves (which were themselves nearly identical). The results with $\beta = 0$ are consistent with an enstrophy cascade at separations below about $\zeta = 0.1$ and an energy cascade from scales of roughly $\zeta = 0.1$ to about $\zeta = 0.8$ (a quarter of the domain). Recall the forcing scales range from $\delta x = \pi/35 - \pi/30$ or from roughly $\delta x = 0.09 - 0.1$. The agreement with the predicted power laws is reasonable, although the slopes are more variable the energy range (reflecting perhaps the slower statistical convergence at larger scales). The transverse and longitudinal curves exhibit the same power laws.

With $\beta = 200$, the longitudinal structure function is very similar to that with $\beta = 0$ except that it falls off faster at larger separations, consistent with an arrest. On the other hand, the curves are nearly identical in the putative enstrophy cascade range.

Higher order structure functions were also calculated. The third order moments were noisy, but exhibited the expected cubic growth with distance in the enstrophy range (e.g. Lindborg, 1999). The linear increase expected in the energy range on the other hand could not be confirmed. Indeed, the dependence at larger separations varied from run to run, suggesting poor statistical convergence.

The normalized fourth order moment (the kurtosis) was Gaussian at most separations

and for all β, but was weakly non-Gaussian in the enstrophy range with β = 0 (but again Gaussian with non-zero β). This would be expected with small-scale intermittency, for instance vortices, which tends to be suppressed by the β-effect (e.g. McWilliams, 1984). Such intermittency need not however alter the ζ^2 dependence of the second order moment in the enstrophy range (Babiano *et al.,* 1985), hence the agreement between the β = 0 and β = 100 curves in Figure 6.

In any case, the velocity structure functions support a cascade from the forcing scales to smaller scales for enstrophy, and to larger scales for energy, with the enstrophy range better resolved than the energy range.

5. Arrest and isotropy

One can gauge the arrest of the inverse cascade using two-point velocity correlations (closely related to the second order structure function). Two-dimensional correlations in particular permit a simultaneous assessment of the dominant length scale and the degree of anisotropy.

The measure to be used is a 2-D correlation "ellipse," constructed as follows: normalized, zero (time) lag, longitudinal and transverse velocity correlations were calculated along the zonal and meridional lines extending from the basin center. These correlations decreased with distance, as is common, and the distances at which each correlation fell below certain values were determined. Those distances were then used to draw ellipses in x and y. Values of 0.8, 0.6 and 0.4 were used for the longitudinal correlation and 0.5 and 0.0 for the transverse (the transverse correlation decreases more rapidly than the longitudinal, and the latter need not cross zero; Batchelor, 1953). The ellipses from the basin center with four values of β are shown in the upper panels of Figure 7.

The ellipses shrink as β is increased, as expected, and the contraction compares favorably with that predicted from relation (6), as indicated by the lines next to the ellipses. To calculate the latter, we need ε, which can be estimated from the total energy. The energy equation is derived from (1) by multiplying by $-\psi$ and averaging over the domain:

$$\frac{\partial}{\partial t} K = \epsilon - 2rK, \tag{12}$$

where K is the total kinetic energy. We assume all energy supplied by the forcing is transferred upscale, that is, that none is lost to small-scale dissipation. At statistical equilibrium then:

$$\epsilon \approx 2rK, \tag{13}$$

so that the arrest scale, from (6), is

$$L_\beta = 2\pi C\beta^{-3/5}(2rK)^{1/5}. \tag{14}$$
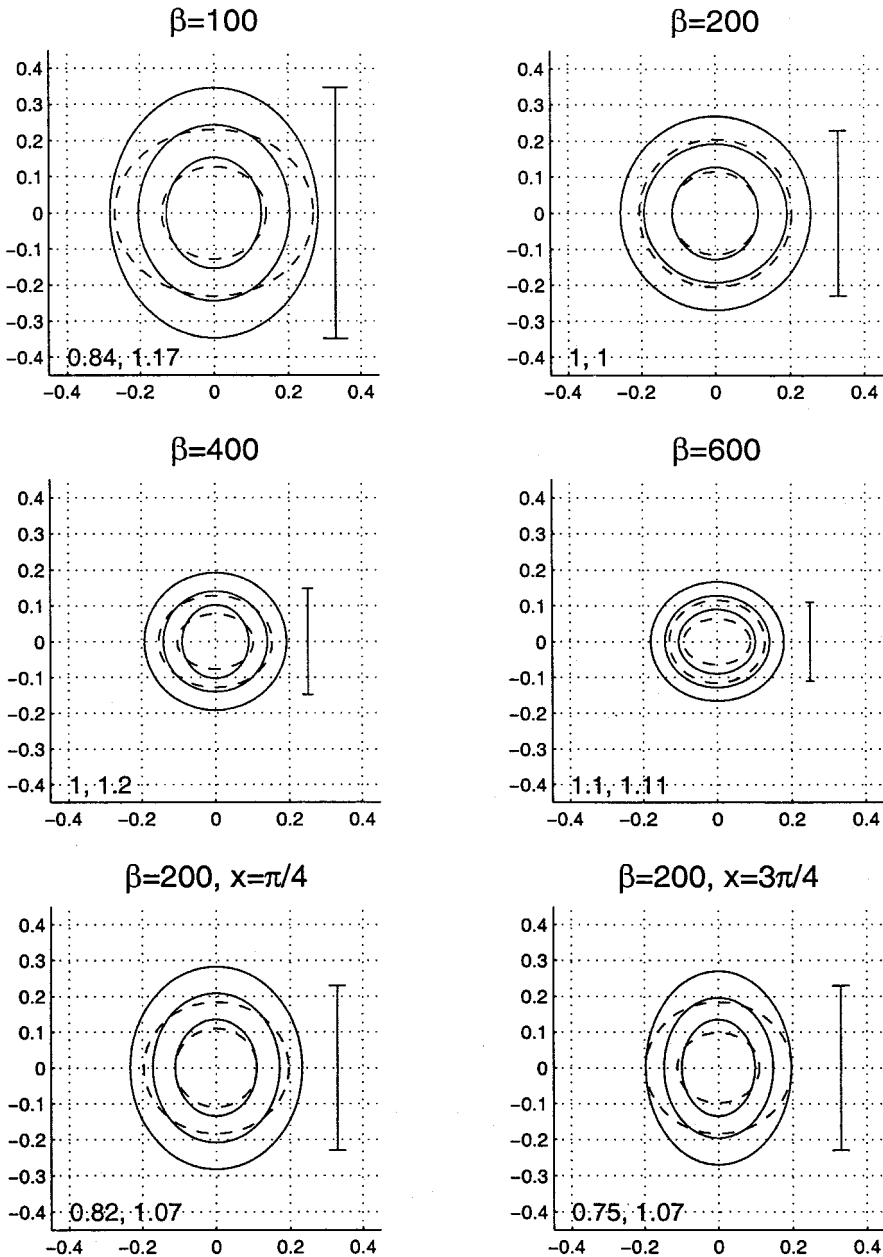
Figure 7. Correlation ellipses for runs with various values of β. The longitudinal ellipses are indicated by solid curves, and represent correlations of [.8 .6 .4]; the transverse correlations are the dashed curves for values of [.5 0]. The ratios of the zonal to meridional axes for the 0.6 longitudinal ellipse and the 0.0 transverse ellipse are given in the lower left corner. The error-type bars have length $2L_\beta$ where L_β is given in (14). The two lower panels show ellipses obtained away from the basin center for $\beta = 200$.
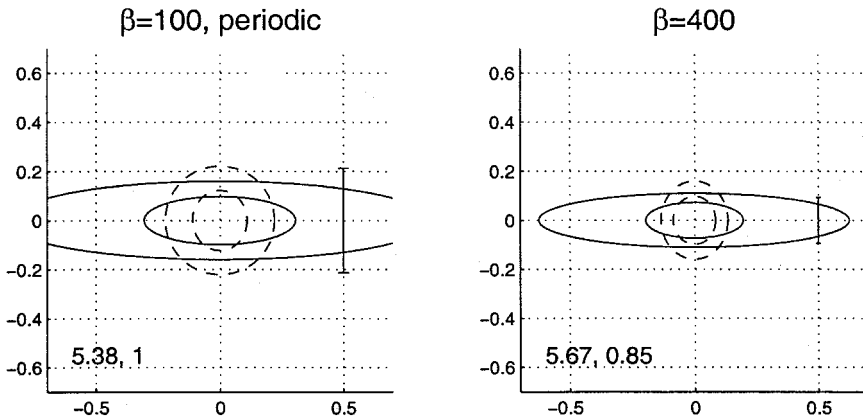
Figure 8. Correlation ellipses for runs with the doubly periodic model with $\beta = 100$ and 400. The format is the same as in Figure 7, except that the .4 longitudinal ellipse has not be drawn.

Note if ϵ is decreased by small-scale dissipation, the term $2rK$ would be decreased by a corresponding fraction. But the resulting change in L_β would be small however because of the 1/5 exponent. The lines in Figure 7 were calculated with $C = 1$, and extend to $\pm L_\beta$.

The decrease in the arrest scale agrees approximately with the decrease in the correlation ellipses, though the former shrink somewhat faster. With $\beta = 600$, the correlation scales are near the forcing scales, indicating the cascade has been largely defeated.

The ellipses are also essentially isotropic. The numbers at lower left in each panel are the ratio of the zonal to meridional major axes, for the longitudinal and transverse ellipses respectively, and these are nearly always one. The meridional decay scales are thus comparable to the zonal decay scales, regardless of β.

How do the ellipses vary with position? The ellipses from $(x, y) = (\pi/4, 0)$ and at $(x, y) = (3\pi/4, 0)$ with $\beta = 200$ (lower two panels of Fig. 7) are nearly the same as at the basin center (top right panel). The longitudinal ellipses imply meridional anisotropy, reflecting most likely the influence of the eastern and western walls, but only a weak anisotropy. The results at other locations, except very near the walls (see below) are likewise similar. So besides being isotropic, the interior is also approximately homogeneous.

The situation is quite different with periodic boundary conditions. Representative ellipses are shown in Figure 8 for two values of β, again with vertical lines indicating the arrest scales. While the transverse correlation ellipses are again nearly isotropic, the longitudinal ellipses are zonally elongated, at both values of β. Both ellipses shrink in y as β is increased, though the change is more pronounced for the transverse correlation. And the estimated arrest scale contracts at a comparable rate, although again somewhat faster than the ellipses.

In this case, the correlations reflect variations in the zonal jets. The transverse correlations in the meridional direction have large negative lobes, due to the alternating

eastward and westward flow; these correlations thus indicate jet width. The longitudinal correlations in the zonal direction gauge the spatial coherence of the jets and in the meridional direction, the north-south jet perturbations. The transverse correlation is thus a better measure of the arrest scale.

Returning to the basin, we can make a further test for isotropy. The longitudinal and transverse correlations are functionally related for isotropic flows; in two dimensions one can show (Batchelor, 1953; Freeland *et al.*, 1975):

$$g(\zeta) = \frac{d}{d\zeta} (\zeta f(\zeta)), \tag{15}$$

where ζ is the separation between points and f and g are the longitudinal and transverse correlations.

For all experiments, relation (15) was evaluated by fitting a seventh-order polynomial to the longitudinal correlation, differentiating its product with ζ and then comparing the result to the transverse correlation; two examples are shown in Figure 9. The predicted curve correctly captures the zero crossings and most of the first negative lobes. Discrepancies occur at larger separations, but these are not statistically significant. Similar results obtain with the other tested values of β.

So the interior fields in the basin are approximately isotropic and homogeneous for the range of values of β tested. If the arguments of Section 1 are correct, the isotropy is related to a spectral arrest to basin modes. In the following section, we seek further evidence of basin modes.

6. Spectra

More can be gleaned from velocity power spectra. These were calculated using a multitaper power spectral density estimation routine (Percival and Walden, 1993), available in the MATLAB software package.

Frequency spectra are used less frequently than wavenumber spectra in the turbulence context. However if the flow is arrested, we might expect the energy to be greatest near:

$$\omega_\beta = C\beta^{2/5}\epsilon^{1/5}, \tag{16}$$

from dimensional considerations and (6). This can be evaluated using (13) if we again neglect energy lost to small scale dissipation.

Consider first the periodic case. Energy spectra in variance preserving form are shown in Figure 10 for two values of β. In these and in the basin spectra, the peak predicted from (16) is also indicated, using an empirically chosen (but fixed) value of $C = (2.5)^{-1}$.

With $\beta = 100$, the meridional energy is peaked near ω_β; the zonal energy is peaked at somewhat lower frequencies. With $\beta = 400$, the meridional energy is also confined to a band of frequencies near ω_β, but the zonal energy is much greater and at lower frequencies. The velocities thus exhibit a zonal anisotropy which increases with β. The "arrest" is
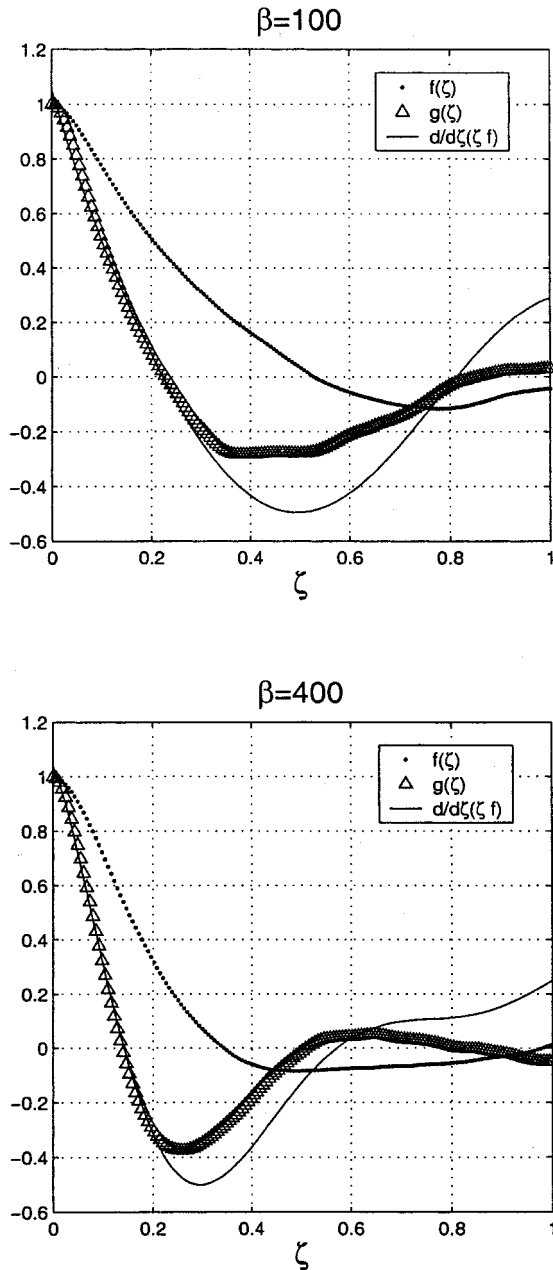
Figure 9. The basin longitudinal (dots) and transverse (triangles) velocity correlations with the transverse correlation predicted from the isotropic relation (15) (solid), at two different values of β.
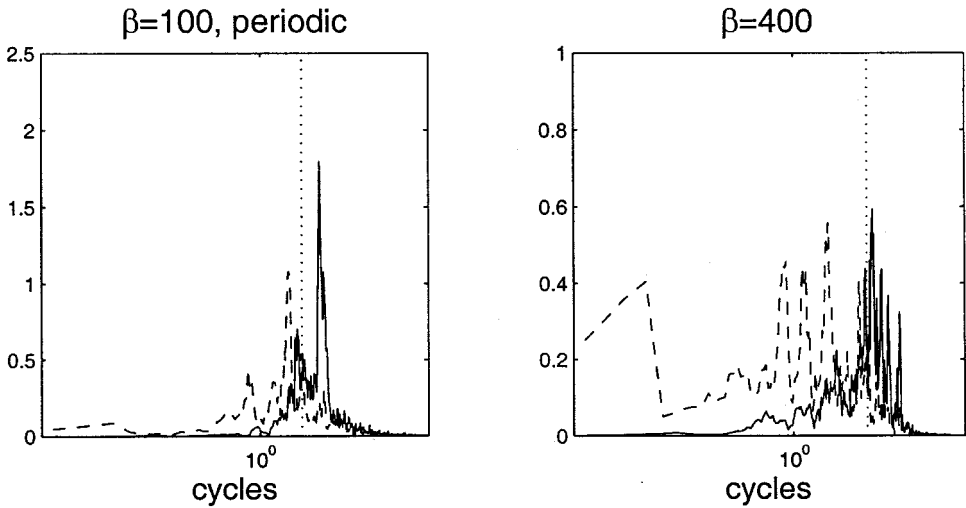
Figure 10. Variance-preserving spectra of the zonal (solid) and meridional (dashed) velocities at the center grid point with the doubly periodic model. Note the abscissa is cycles/unit time, or $\omega/(2\pi)$.

clearer in the meridional spectra rather than the zonal (see also Rhines, 1975; Vallis and Maltrud, 1993).

With the basin spectra (upper and middle panels of Fig. 11), the meridional energy is likewise peaked near ω_β. But now the zonal energy is confined to approximately the same frequency band. The basin interior is more isotropic from the spectral perspective as well.

In addition, the basin spectra exhibit definite peaks. These are seen in both the meridional and zonal spectra, but are often clearer in the former. They occur at frequencies which correspond to barotropic basin modes, as calculated from (5) (dashed lines). The excited modes have larger wavenumbers with larger values β and in addition have unequal zonal and meridional wavenumbers (the zonal wavenumber has been taken to be the smaller, for reasons described later). Griffa and Castellari (1991) documented similar spectral peaks and likewise attributed them to basin modes.

The spectra at other locations are very similar, although the peak amplitudes vary. Where they do differ is near the boundaries; two examples, near the eastern and northern boundary with $\beta = 200$, are shown in the lower panels of Figure 11. Not surprisingly, the zonal variance is greatly suppressed near the eastern wall and the meridional variance suppressed near the northern wall. The eastern wall spectrum still exhibits a mode (1, 3) peak, but no peaks are evident at the northern wall. Of interest is that the spectra at $(x, y) = (3.0, 1.57)$ and $(x, y) = (1.57, 3.0)$ are nearly the same as at the basin center.

The spectra thus also support an approximately isotropic and homogeneous interior, and exhibit peaks consistent with basin modes. Before considering the latter in more detail, we examine one more aspect of the arrested wave field.
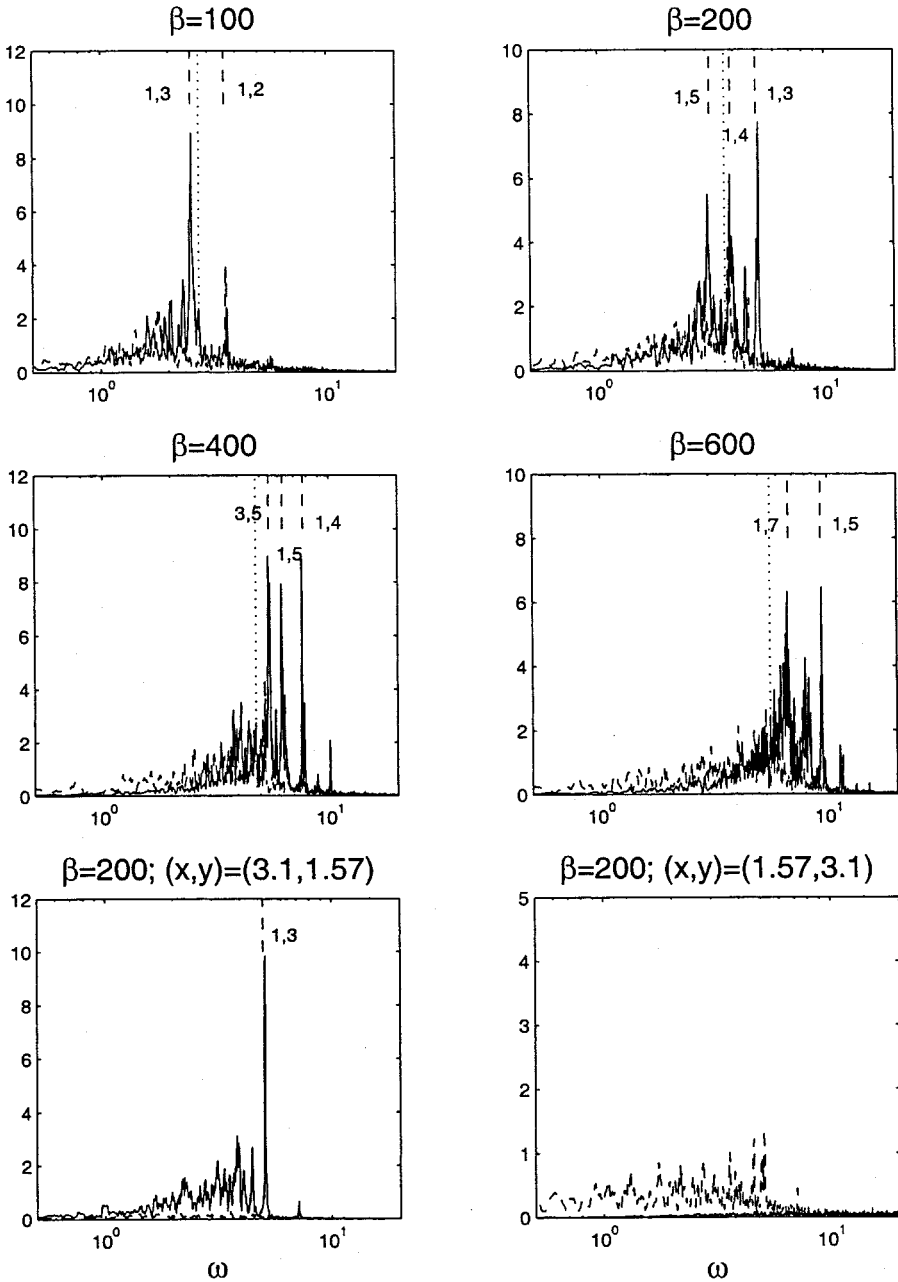
Figure 11. Variance-preserving spectra of the meridional velocities in the basin for four values of β (upper panels). Superimposed are lines indicating the frequencies of certain basin normal modes. The lower panels show spectra obtained near the eastern and western walls with β = 200.

Meridional velocity at x=2.31 (solid) and 2.06 (dashed), β=100

β=400

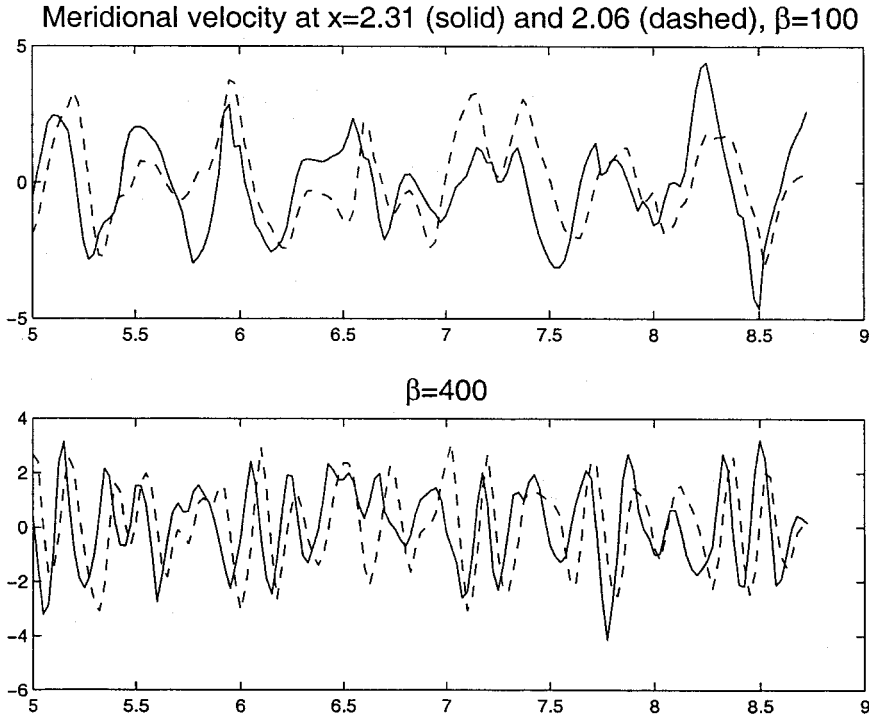Figure 12. Examples of the meridional velocity time series obtained at two separate points on the zonal line with $\beta = 100$ and 400. Note the eastern time series (solid) lag the western (dashed) ones and that the lag does not change appreciably with β (though the dominant frequency does).

7. Phase propagation

If the interior is wave-like, we should see westward phase propagation; this applies to basin modes as well (see 18). The observed phase speed moreover should not vary with β but rather with the rms velocity.

Time-longitude (Hovmuller) plots constructed from the streamfunction fields indicate westward phase propagation (not shown). This is clearer with the smaller values of β than with the larger values, but in all cases, the inferred phase speed is approximately $c_p = -4.0$, or roughly 2–2.5 times the rms velocity (given below).

More robust phase speed estimates can be obtained from the velocity records along the basin equator. Portions of the meridional velocity time series from two locations closely spaced on the line are shown in Figure 12 and the phase lag at the western-most observer is clear with both smaller and larger values of β. The phase shift moreover is approximately the same for both values of β (despite the higher dominant frequency in the latter case).

Phase speeds can be calculated from spatially-lagged cross correlations, by dividing the spacing between observations by the time lag. The results for a lag of $2\delta t$ (where δt was the temporal resolution of the record) from the basin center are shown in Table 1. We note the

Table 1. Phase velocities determined from cross correlations of the velocity records along the zonal central line. The separations are in terms of $\delta x = \pi/512$. The correlation is shown in the penultimate column, and the implied phase speed in the last.

β	Vel.	Rms	Sep. ($\times \delta x$)	Corr.	c_p
100	u	1.77	29	0.65	3.56
100	v	2.03	19	0.62	2.33
200	u	1.55	30	0.63	3.68
200	v	2.03	23	0.61	2.82
400	u	1.63	32	0.59	3.93
400	v	1.93	27	0.52	3.31
600	u	1.56	32	0.44	3.93
600	v	1.76	28	0.42	3.44

correlations were typically higher (near 0.8) at a lag of δt, and lower (near 0.4) at a lag of $3\delta t$.

The dominant phase speed does not vary greatly with β and is generally 1.5–2 times the rms velocity. There is an increase in the phase speeds which is not mirrored in the rms velocities, but this is small and within the errors. There is also a slight decrease in correlation with β, due presumedly to the increase in higher frequency variability. The phase speeds inferred from the meridional velocities are smaller than those from the zonal velocities, and it is not immediately apparent why (though as noted in Section 6, the meridional spectra exhibit clearer peaks than the zonal spectra). We observe no variation of phase speed along the zonal line, e.g. the results relative to the records at $x = 2.80$ are identical within error to those relative to $x = 1.57$.

We can compare the phase speeds with those of the basin modes indicated in the frequency spectra (Fig. 11). The basin mode phase speed (see below) is:

$$c_p = -\frac{2\omega^2}{\beta}. \tag{17}$$

For $\beta = 100$, the phase speed of mode (2, 3) is -3.85; for $\beta = 400$, $c_p(1, 7) = -4.0$. These are roughly consistent with Table 1 and with those inferred from time-longitude plots.

8. Basin modes

The results suggest an arrest occurs to basin modes whose dominant phase speeds are proportional to the rms velocity. However, several questions arise regarding this interpretation. First, why do the excited modes have unequal zonal and meridional wavenumbers (Fig. 11)? Second, can the modes be expected to exist with the bottom drag? And third, why are their frequencies unaltered by the mean flow?

First, basin modes with $n \ll m$ are more nearly isotropic than those with $n \approx m$ or with

$n \gg m$. Basin modes have a dual structure, part standing wave and part propagating wave (e.g. Longuet-Higgins, 1964):

$$\psi \propto \cos\left(\frac{\beta}{2\omega_{nm}}x - \omega_{nm}t\right) \sin(nx) \sin(my), \tag{18}$$

where we have taken $L_x = L_y = \pi$; ω_{nm} is given in (5). The mode has a meridional wavelength of π/m, but the zonal wavelength is not simply π/n because the propagating portion has a wavelength:

$$\frac{2\pi\omega_{nm}}{\beta} \propto \frac{\pi}{(n^2 + m^2)^{1/2}}. \tag{19}$$

This means that the more isotropic basin modes have small n. Two such modes (whose frequencies match peaks in Figure 11) are contoured in the middle and lower right panels of Figure 13.[6]

The second question concerns the bottom drag, which can severely degrade basin modes. A basin mode can be written as the sum of four free Rossby waves, two with a westward group velocity and two with an eastward velocity (Longuet-Higgins, 1964). The eastward waves are generally the slower and hence more susceptible to dissipation. The four free waves have wavenumbers:

$$(k, l) = \left(-\frac{\beta}{2\omega_{mn}} \pm m, \pm n\right) = ((m^2 + n^2)^{1/2} \pm m, \pm n), \tag{20}$$

from which we derive the group velocities:

$$c_g = \frac{\beta(k^2 - l^2)}{(k^2 + l^2)^2} = \frac{\beta m(m \pm (m^2 + n^2)^{1/2})}{2(m^2 + n^2 \pm m(m^2 + n^2)^{1/2})^2}. \tag{21}$$

For the $(1, 3)$ mode with $\beta = 100$ (Fig. 11), the group velocities are 1.2 and -2.3. Multiplying these by the e-folding time of the damping, $1/r = 10$, yields distances much greater than the basin width, $L = \pi$, implying the eastward waves could easily transit the basin with the given dissipation. Hence basin modes are plausible. The velocities for the $(1, 5)$ mode with $\beta = 400$ are 1.3 and -1.9, so the conclusion is the same.

The last question is whether the mean flow alters the modal frequencies. As noted in Section 3, the mean flows have velocities comparable to the observed phase speeds (Sec. 7), suggesting the mean could have a large impact. But the mean gyres are strongly trapped at the northern and southern boundaries and so may have little effect in the interior.

6. An alternate method exists for identifying basin modes in a given streamfunction field, and even whether $n < m$ or $n > m$. Because the set of basin modes comprises a complete, orthogonal basis, one can use them to decompose a given streamfunction (Pedlosky, 1987). The decomposition was applied to several of the present streamfunction fields and the results generally supported those from the frequency spectra (Fig. 11) for the smaller values of β. The results however were less satisfactory with the larger β. The latter discrepancy stemmed from the western boundary layer, which projected onto basin modes with short zonal scales (the western layer is relatively less prominent at smaller β). The implied strong *meridional* anisotropy was of course not observed in the interior.
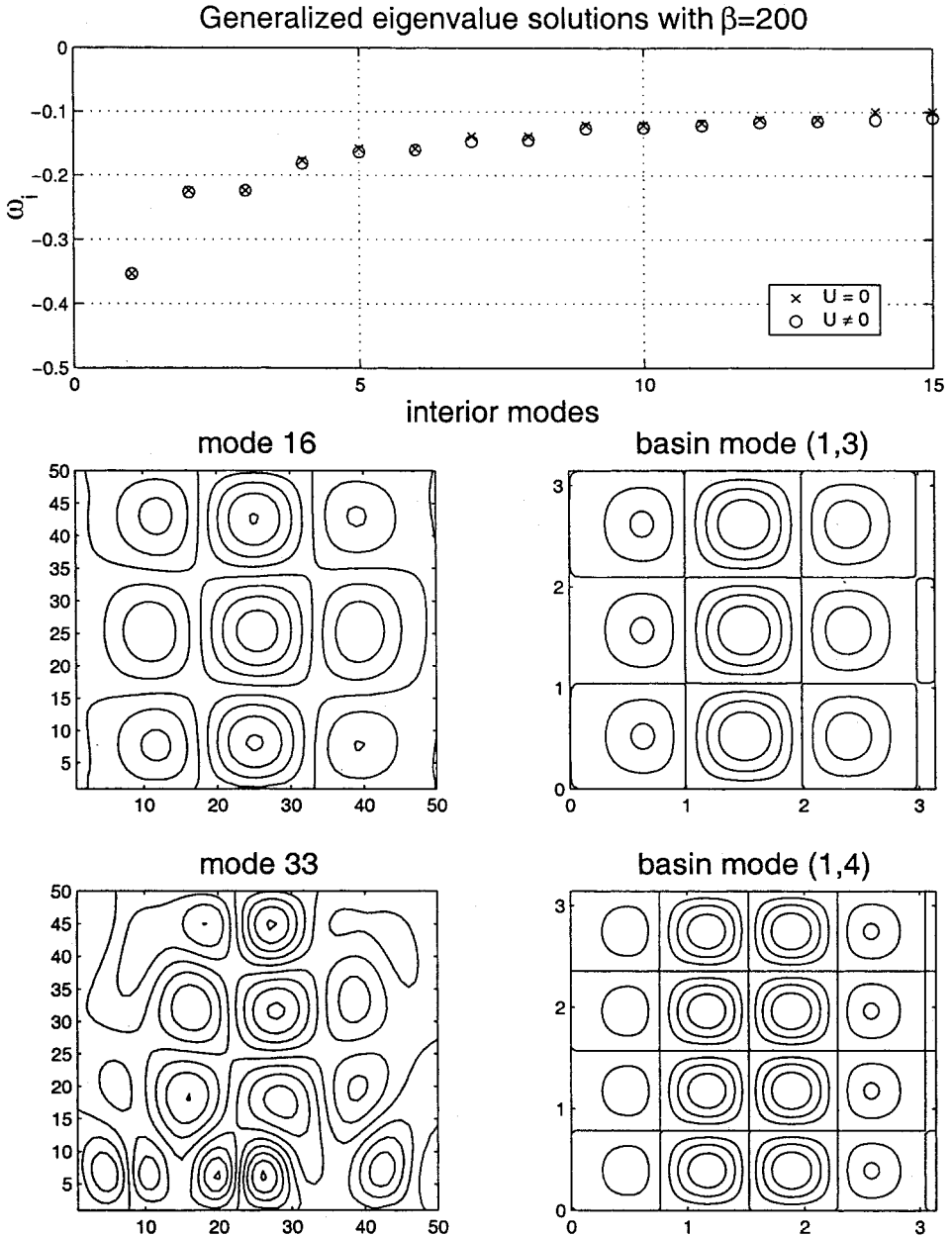
Figure 13. Numerical basin mode solutions from the generalized eigenvalue problem with the mean flow obtained in the basin with β = 200. The modal frequencies are shown in the upper panel, with those expected with zero mean. The middle and lower left panels show two eigenvectors obtained, and the middle and lower right panels their zero mean counterparts.

To address the mean-induced alterations, we resort to a linear calculation. The basin modes in the presence of a mean like that in the experiments can be obtained by solving the generalized eigenvalue problem:

$$i\omega \mathbf{A}\psi = \mathbf{B}\psi, \tag{22}$$

where $\mathbf{A} \equiv \nabla^2$ and $\mathbf{B} \equiv \beta\partial_x + U(x, y)\partial_x\nabla^2 + V(x, y)\partial_y\nabla^2$. This was done numerically, using the mean velocities interpolated from the model fields and using center differences for the derivatives. For the calculation, time was rescaled by β^{-1} so that the mean velocity was also divided by β. The MATLAB shifted Arnoldi routine for sparse matrices was used to obtain the eigenvalues and eigenvectors and a 50 by 50 grid was used (although the results for the gravest modes are quantitatively similar with fewer grid points).

The results for the case with $\beta = 200$ are shown in Figure 13. Shown in the upper panel are the frequencies for the first 15 basin modes, with and without the mean flow; in the middle and lower left panels are two sample eigenvectors and in the adjacent right panels the corresponding zero-mean modes. Note the gravest (zero mean) basin mode has a scaled frequency of $\omega = -(2\sqrt{2})^{-1}$.

From the upper panel, we see the mean flow alters the gravest mode frequencies very little. The dominant modes in Figure 11 would see their frequencies change by at best a few percent. From the lower panels, we see the mean likewise alters the modal structures minimally. The (1, 3) mode is nearly unchanged; the (1, 4) mode is distorted somewhat near the northern and southern boundaries, but the overall structure is largely the same. One finds greater changes in modes with larger meridional wavenumbers but the modes corresponding to the peaks in Figure 11 are relatively unaffected.

The mean has relatively little impact because it is confined. For modes of large meridional extent, the gyres merely tilt the streamfunction in their vicinity; only when a mode's meridional wavelength is much smaller than the gyre width is the mode more profoundly altered. But because the *dominant* modes at arrest have a meridional scale which is comparable to that of the gyres (Fig. 4), those modes are not greatly affected.

With a smaller value of β, the (scaled) mean is stronger, but at the same time the excited modes are larger in scale. Conversely, if β is larger, higher modes are excited but the scaled mean is weaker. In neither case does the mean greatly alter the arrested modes.

The modes with small scales are strongly affected, and many become trapped in the gyre regions. These modes represent oscillations in the gyres themselves and have frequencies comparable to the graver zero-mean modes (their frequencies were excluded in the upper panel). But because they do not extend into the interior, they have minimal effect on the variability there.

9. Summary and discussion

We have revisited geostrophic turbulence forced at small scales in a square basin with β. The inverse cascade is not halted by enstrophy production at the western wall, consistent

with previous indications. The cascade "arrests" due to competition from Rossby waves, as in a periodic domain. But basin modes rather than free waves evidently brake the cascade. The indirect evidence for modes is that the arrested interior is approximately isotropic; the direct evidence is that there are peaks in the Eulerian spectra at frequencies matching modal frequencies. The basin interior is also approximately homogeneous, and one sees no zonal jets there (in stark contrast to periodic domains).

The rectified mean flow in these experiments is in line with theoretical expectations (Salmon *et al.*, 1976; Bretherton and Haidvogel, 1976) and with previous numerical experiments. The observed $\langle q \rangle - \langle \psi \rangle$ relation is linear with a positive slope in the region of the gyres; $\langle \psi \rangle$ is approximately zero outsize the gyres. Of interest is that with the present model has implicit small scale damping, with a viscosity parallel to the local velocity and with no boundary conditions imposed on the vorticity. No vorticity homogenization occurs in the mean gyres, in contrast to previous studies where explicit diffusion or hyperdiffusion was used.

The bottom drag and the rectified mean could conceivably have altered or even suppressed basin modes. However, we showed that the excited modes had free wave components which were too fast to be appreciably damped, and that the means were too weak and spatially confined to alter the modes (Sec. 8). Presumedly if the drag is small enough to permit a cascade in the first place, the modes will be similarly unaffected.

In Section 1 we suggested the arrest to basin modes might be isotropic because the modal dispersion relation is symmetric in n and m. But the excited modes must also have $n \ll m$ to be symmetric! This curious discrepancy suggests that while the phenomenological argument, which considers only time scales, is correct in essence, the actual situation is more subtle. A more complete theory is clearly required, for instance a disequilibrium statistical mechanics treatment (Holloway, 1986).

Turbulent velocity fields are typically characterized in terms of wavenumber spectra, but the boundary-trapped vorticity anomalies adversely affect the spatial averages required for such spectra. Fortunately one can capture the various turbulence characteristics using only Eulerian velocity statistics, such as structure functions, power spectra, and velocity correlations. It should be emphasized that the two approaches are complimentary; for example the second order structure function is directly related to the energy spectrum (e.g. Babiano *et al.*, 1985). Similar velocity statistics might also be used to advantage in the subsurface ocean.

We have emphasized the isotropy of the interior fields, but our forcing was isotropic and the basin square. Anisotropic forcing and (possibly) a rectangular basin could conceivably produce anisotropy. Seidov and Marushkevich (1992) for example describe zonally elongated eddies in simulations conducted in a meridionally-elongated basin. Having unequal zonal and meridional basin widths would break the symmetry between meridional and zonal wavenumbers in the basin mode dispersion relation, perhaps favoring anisotropy in one direction or the other. The arrest could likewise be changed if the basin modes were altered, for example by large scale topography (e.g. Anderson *et al.*, 1979).

The present results also stem in part from the choice of homogeneous forcing. Spatially isolated forcing can generate zonally-elongated structures (Haidvogel and Rhines, 1983); indeed, if the forcing region is small and far from the boundaries, the situation must be like that on an infinite plane, with free Rossby waves rather than basin modes countering the (local) cascade. With the forcing applied over the whole domain, the boundaries are evidently important at all times (i.e. there was no indication of even transient zonal anisotropy).

Are the present findings at all relevant to the ocean? There is a recent set of observations which show some encouraging similarities. Warren *et al.* (2002) examined a (zonal) line of current meters in the Mascarene basin of the Indian Ocean, and these records were dominated by a barotropic fluctuation with a 59 day period whose phase propagated westward. Of interest is that: (1) the wave phase speed was comparable to the peak to peak velocity, (2) the wave speed and frequency (from spectra) matched the second basin mode and (3) the current meter spectra exhibited a dominant peak. All three aspects are in accord with the present results. Warren *et al.* wondered why mode 1 was absent, but this could be explained if a cascade were arrested at the second mode. Of course there are discrepancies, for instance the Mascarene wave had much greater meridional than zonal velocities (which may be related to the basin's shape). Likewise, our spectra suggest multiple modes at arrest, but this too might stem from differences in forcing, basin geometry and/or dissipation.

We have framed the present discussion in terms of an arrested cascade, but at least one alternate interpretation is possible. Manfroi and Young (1999) have recently shown that zonal jets in a periodic domain can be generated by a large scale shear instability with small scale, stationary forcing; such an instability can be seen as a highly nonlocal inverse cascade. In their case the jet scale depends on bottom friction but *not* on the Rhines scale. It is intriguing to wonder whether and how such an instability might operate in the closed domain. Our results do suggest a dependence on the Rhines scale, so the basin might prove an interesting test for their proposition. This is WHOI contribution number 10470.

REFERENCES

Anderson, D. L. T., K. Bryan, A. E. Gill and R. C. Pacanowski. 1979. The transient response of the North Atlantic — some model studies. J. Geophys. Res., *84,* 4795–4815.

Babiano, A., C. Basdevant and R. Sadourny. 1985. Structure functions and dispersion laws in two-dimensional turbulence. J. Atmos. Sci., *42,* 942–949.

Batchelor, G. K. 1953. The Theory of Homogeneous Turbulence. Cambridge University Press, 197 pp.

Becker, J. M. and R. Salmon. 1997. Eddy formation on a continental slope. J. Mar. Res., *55,* 181–200.

Bretherton, F. B. and D. Haidvogel. 1976. Two-dimensional turbulence over topography. J. Fluid Mech., *78,* 129–154.

Carnevale, G. F. and J. D. Fredericksen. 1987. Nonlinear stability and statistical mechanics of flow over topography. J. Fluid Mech., *175,* 157–181.

Cessi, P., G. R. Ierley and W. R. Young. 1987. A model of the inertial recirculation driven by potential vorticity anomalies. J. Phys. Oceanogr., *17,* 1640–1652.

Cho, J. and L. M. Polvani. 1996. The formation of jets and vortices from freely-evolving shallow water turbulence on the surface of a sphere. Phys. Fluids, *8,* 1531–1552.

Colin de Verdiere. 1980. Quasi-geostrophic turbulence in a rotating homogeneous fluid. Geophys. Astrophys. Fluid Dyn., *15,* 213–251.

Cummins, P. F. 1992. Inertial gyres in decaying and forced geostrophic turbulence. J. Mar. Res., *50,* 545–566.

Dukowicz, J. K. and R. J. Greatbatch. 1999. Evolution of mean-flow Fofonoff gyres in barotropic quasigeostrophic turbulence. J. Phys. Oceanogr., *29,* 1832–1852.

Ferziger, J. H. and M. Peric. 1999. Computational Methods for Fluid Dynamics. Springer-Verlag, 400 pp.

Fjørtoft, R. 1953. On the changes in the spectral distribution of kinetic energy for twodimensional, nondivergent flow. Tellus, *5,* 225–230.

Fofonoff, N. P. 1954. Steady flow in a frictionless homogeneous ocean. J. Mar. Res., *13,* 254–262.

Freeland, H. J., P. B. Rhines and T. Rossby. 1975. Statistical observations of the trajectories of neutrally buoyant floats in the North Atlantic. J. Mar. Res., *33,* 383–404.

Frisch, U. 1995. Turbulence, Cambridge Univ. Press, 296 pp.

Greatbatch, R. J. and B. T. Nadiga. 2000. Four-gyre circulation in a barotropic model with double-gyre wind forcing. J. Phys. Oceanogr., *30,* 1461–1471.

Griffa, A. and S. Castellari. 1991. Nonlinear general circulation of an ocean model driven by a wind with a stochastic component. J. Mar. Res., *49,* 53–73.

Griffa, A. and R. Salmon. 1989. Wind-driven ocean circulation and equilibrium statistical mechanics. J. Mar. Res., *47,* 457–492.

Haidvogel, D. and P. B. Rhines. 1983. Waves and circulation driven by oscillatory winds in an idealized ocean basin. Geophys. Astrophys. Fluid Dyn., *25,* 1–65.

Holloway, G. 1986. Eddies, waves, circulation and mixing: statistical geofluid mechanics. Ann. Rev. Fluid Mech., *18,* 91–147.

Holloway, G. and M. C. Hendershott. 1977. Stochastic closure for nonlinear Rossby waves. J. Fluid Mech., *141,* 27–50.

Huang, H. and W. A. Robinson. 1998. Two-dimensional turbulence and persistent zonal jets in a global barotropic model. J. Atmos. Sci., *55,* 611–632.

Kolmogorov, A. N. 1941a. The local structure of turbulence in incompressible viscous fluid for very large Reynolds number. Dokl. Akad. Nauk SSSR, *30,* 9–13.

—— 1941b. Dissipation of energy in locally isotropic turbulence. Dokl. Akad. Nauk SSSR, *32,* 16–18.

Kraichnan, R. H. 1967. Inertial ranges of two dimensional turbulence. Phys. Fluids, *10,* 1417–1423.

Kraichnan, R. and D. Montgomery. 1980. Two-dimensional turbulence. Rep. Prog. Phys., *43,* 547–619.

Lele, 1992. Compact finite difference schemes with spectral-like resolution. J. Comp. Phys., *103,* 16–42.

Leonard, B. P. 1979. A stable and accurate convection modelling procedure based on quadratic upstream interpolation. Comp. Meth. Appl. Mech. Eng., *19,* 59–98.

Lindborg, E. 1999. Can the atmospheric kinetic energy spectrum be explained by two-dimensional turbulence? J. Fluid Mech., *388,* 259–288.

Longuet-Higgins, M. S. 1964. Planetary waves on a rotating sphere. Proc. R. Soc. London, Ser. A, *279,* 446–473.

Manfroi, A. J. and W. R. Young. 1999. Slow evolution of zonal jets on the Beta plane. J. Atmos. Sci., *56,* 784–800.

Marshall, J. C. 1984. Eddy-mean flow interaction in a barotropic ocean model. Quart. J. Roy. Meteor. Soc., *110,* 573–590.

McWilliams, J. C. 1984. The emergence of isolated coherent vortices in turbulent flow. J. Fluid Mech., *146,* 21–43.

McWilliams, J. C., W. R. Holland and J. H. S. Chow. 1978. A description of numerical Antarctic Circumpolar currents. Dyn. Atmos. Oceans, *2,* 213–291.

Nozawa, T. and S. Yoden. 1997. Formation of zonal band structures in forced two-dimensional turbulence on a rotating sphere. Phys. Fluids, *9,* 2081–2093.

Onsager, L. 1949. Statistical hydrodynamics. Nuovo Cimento Supp., *6,* 279–287.

Panetta, R. L. 1993. Zonal jets in wide baroclinically unstable regions: persistence and scale selection. J. Atmos. Sci., *50,* 2073–2106.

Patterson, G. S. and S. A. Orszag. 1971. Spectral calculations of isotropic turbulence: efficient removal of aliasing interactions. Phys. Fluids, *14,* 2538–2541.

Pedlosky, J. 1965. A study of the time dependent ocean circulation. J. Atmos. Sci., *22,* 267–272.

—— 1987. Geophysical Fluid Dynamics, Springer-Verlag, 710 pp.

Percival, D. B. and A. T. Walden. 1993. Spectral Analysis for Physical Applications: Multitaper and Conventional Univariate Techniques, Cambridge Univ. Press, 583 pp.

Rhines, P. B. 1975. Waves and turbulence on a beta-plane. J. Fluid Mech., *69,* 417–443.

—— 1979. Geostrophic Turbulence. Ann. Rev. Fluid Mech., *11,* 401–41.

—— 1994. Jets. Chaos, *4,* 313–339.

Rhines, P. B. and W. R. Young. 1982. Homogenization of potential vorticity in planetary gyres. J. Fluid Mech., *122,* 347–367.

Sadourny, R. and C. Basdevant. 1985. Parameterization of subgrid scale barotropic and baroclinic eddies in quasigeostrophic models. Anticipated potential vorticity method. J. Atmos. Sci., *42,* 1355–1363.

Salmon, R., G. Holloway and M. C. Hendershott. 1976. The equilibrium statistical mechanics of simple quasi-geostrophic models. J. Fluid Mech., *75,* 691–703.

Seidov, D. G. and A. D. Marushkevich. 1992. Order and chaos in ocean current dynamics: numerical experiments. Dyn. Atmos. Oceans, *16,* 405–434.

Shchepetkin, A. F. and J. C. McWilliams. 1998. Quasi-monotone advection schemes based on explicit, locally adaptive dissipation. Mon. Weather Rev., *126,* 1541–1580.

Shepherd, T. G. 1987. Non-ergodicity of inviscid two-dimensional flow on a beta-plane and on the surface of a rotating sphere. J. Fluid Mech., *184,* 289–302.

Spall, M. A. 2000. Generation of strong mesoscale eddies by weak ocean gyres. J. Mar. Res., *58,* 97–116.

Stommel, H. 1948. The westward intensification of wind-driven ocean currents. Trans. Am. Geophys. Union, *29,* 202–206.

Treguier, A. M. and J. C. McWilliams. 1990. Topographic influences on wind-driven, stratified flow in a β-plane channel: an idealized model for the Antarctic Circumpolar Current. J. Phys. Oceanogr., *20,* 321–343.

Vallis, G. K. and M. E. Maltrud. 1993. Generation of mean flows and jets on a beta-plane and over topography. J. Phys. Oceanogr., *24,* 1346–1362.

Van Atta, C. W. and W. Y. Chen. 1970. Structure functions of turbulence in the atmospheric boundary layer over the ocean. J. Fluid Mech., *44,* 145–159.

Van Atta, C. W. and J. T. Park. 1980. Hot- and cold-wire sensitivity corrections for moments of the fine scale turbulence velocity derivatives. Phys. Fluids, *23,* 701–705.

Veronis, G. 1966. Wind-driven ocean circulation—part 2: numerical solutions of the non-linear problem. Deep-Sea Res., *13,* 31–55.

—— 1970. Effect of fluctuating winds on ocean circulation. Deep-Sea Res., *17,* 421–434.

Wang, J. and G. K. Vallis. 1994. Emergence of Fofonoff states in inviscid and viscous ocean circulation models. J. Mar. Res., *52,* 83–127.

Warren, B. A., T. Whitworth and J. H. LaCasce. 2002. Forced resonant undulation in the Deep Mascarene Basin. Deep-Sea Res., *49,* 1513–1526.

Williams, G. P. 1978. Planetary circulations I: barotropic representation of Jovian and terrestrial turbulence. J. Atmos. Sci., *35,* 1399–1426.